

## Dynamics of $H^+ + N_2$ at $E_{Lab} = 30$ eV

Christopher Stopera, Buddhadev Maiti,<sup>a)</sup> Thomas V. Grimes, Patrick M. McLaurin, and Jorge A. Morales<sup>b)</sup>

Department of Chemistry and Biochemistry, Texas Tech University, PO Box 41061, Lubbock, Texas 79409-1061, USA

(Received 15 March 2011; accepted 19 May 2011; published online 14 June 2011)

The  $H^+ + N_2$  system at  $E_{Lab} = 30$  eV, relevant in astrophysics, is investigated with the simplest-level electron nuclear dynamics (SLEND) method. SLEND is a time-dependent, direct, variational, non-adiabatic method that employs a classical-mechanics description for the nuclei and a single-determinantal wavefunction for the electrons. A canonical coherent-states procedure, intrinsic to SLEND, is used to reconstruct quantum vibrational properties from the SLEND classical mechanics. Present simulations employ three basis sets: STO-3G, 6-31G, and 6-31G\*\*, to determine their effect on the results, which include reaction visualizations, product predictions, and scattering properties. Present simulations predict non-charge-transfer scattering and  $N_2$  collision-induced dissociation as the main reactions. Average vibrational energy transfer,  $H^+$  energy-loss spectra, rainbow angle, and elastic vibrational differential cross sections at the SLEND/6-31G\*\* level agree well with available experimental data. SLEND/6-31G\*\* results are comparable to those calculated with the vibrational close-coupling rotational infinite-order sudden approximation and the quasi-classical trajectory method. © 2011 American Institute of Physics. [doi:10.1063/1.3598511]

### I. INTRODUCTION

Research on gas-phase proton-molecule reactions is of primary importance in theoretical and experimental chemistry. The relevance of those reactions arises from their prevalence in the upper atmosphere, astrophysical media, plasmas, particle accelerators, and cancer proton therapy. Consequently, numerous proton-molecule reactions (e.g.,  $H^+ + M$ , with  $M = H_2$ ,<sup>1,2</sup>  $N_2$ ,<sup>2-5</sup>  $O_2$ ,<sup>2,4,6</sup>  $CO$ ,<sup>3-5</sup>  $HF$ ,<sup>3,7</sup>  $HCl$ ,<sup>3</sup>  $H_2O$ ,<sup>8</sup>  $CO_2$ ,<sup>2,7,9</sup>  $N_2O$ ,<sup>9</sup>  $CH_4$ ,<sup>10</sup>  $C_2H_2$ ,<sup>11</sup>  $CF_4$ ,<sup>12</sup>  $SF_6$ ,<sup>12</sup> etc.) have been investigated in cross-beam scattering experiments. Those experiments provided accurate state-to-state properties of the investigated reactions and stimulated theoretical research on some of them (cf. Ref. 1 and 13, and 14).

Among several proton-molecule reactions,  $H^+ + N_2$  at intermediate collision energies (i.e.,  $\sim 10$  eV  $\leq E_{Lab} \leq 500$  eV) has attracted considerable attention due to its contribution to the  $N_2H^+$  formation in interstellar clouds.<sup>15</sup> Therefore, the  $H^+ + N_2$  reaction has been studied experimentally<sup>2-5</sup> at collision energies ranging from  $E_{Lab} = 9.8$  eV (Ref. 4) to 166 eV (Ref. 2) ( $E_{c.m.} = 9.5$  eV (Ref. 4) to 160 eV (Ref. 2)). Those experiments revealed that  $H^+ + N_2$  exhibits a considerable inertia to undergo collision-induced vibrational excitations and electron-transfer reactions. At most collision energies, only two vibrational channels,  $H^+ + N_2 (v_i = 0) \rightarrow H^+ + N_2 (v_f = 0 - 1)$  were detected, with a clear predominance of the elastic one ( $v_f = 0$ ). Only at the relatively high energy of  $E_{Lab} = 149$  eV ( $E_{c.m.} = 144$  eV),<sup>2</sup> were excitations with  $v_f = 2$  clearly detected. The vibrational behavior of  $H^+ + N_2$  differs markedly from those of the re-

lated systems:  $H^+ + H_2$ ,<sup>1</sup>  $H^+ + O_2$ ,<sup>6</sup> and  $H^+ + CO^5$  at  $E_{Lab} = 30$  eV, which exhibit excitations with  $v_f$  up to 6 ( $H_2$ ), 4 ( $O_2$ ), and 2 ( $CO$ ).

The most comprehensive experiment on  $H^+ + N_2$  at intermediate collision energies was conducted by Krutein and Linder<sup>5</sup> at  $E_{Lab} = 30$  eV, with a few additional measurements at  $E_{Lab} = 50$  and 79.8 eV. That experiment was part of a comparative study among the related systems:  $H^+ + N_2$ ,  $H^+ + CO$ , and  $H^+ + NO$ . For  $H^+ + N_2$  at  $E_{Lab} = 30$  eV, Krutein and Linder determined projectile energy-loss spectra that, similarly to other experiments, revealed only two vibrational channels,  $H^+ + N_2 (v_i = 0) \rightarrow H^+ + N_2 (v_f = 0 - 1)$  with the elastic one ( $v_f = 0$ ) clearly favored. The measured energy-loss spectra allowed the determination of the average vibrational energy transfer and of differential cross sections (DCS) for the elastic channel.

The Krutein and Linder experiment on  $H^+ + N_2$  at  $E_{Lab} = 30$  eV has become the obligatory standard to appraise theoretical studies of that system. Early attempts at simulating  $H^+ + N_2$  were hindered by the lack of  $H^+ - N_2$  potential energy surfaces (PESs).<sup>16</sup> Eventually, ground-state PESs for that system became available and two important theoretical studies of the Krutein and Linder experiment were conducted. The first study by Gianturco *et al.*<sup>17</sup> employed the quantum-mechanical vibrational close-coupling rotational infinite-order sudden (VCC-RIOS) approximation on a  $H^+ - N_2$  ground-state PES at the multireference double-excitation configuration interaction (MRDCI) level. The second study by Ritschel *et al.*<sup>16</sup> employed quasi-classical trajectory (QCT) dynamics on two fits of a  $H^+ - N_2$  ground-state MRDCI PES, henceforth, denoted PES I and PES II, respectively. Overall, both studies reproduced well many of the results of the Krutein and Linder experiment but at the considerable cost of constructing complete high-level PESs.

<sup>a)</sup>Present address: Department of Chemistry, Georgia State University, Atlanta, Georgia 30302-4098, USA.

<sup>b)</sup>Author to whom correspondence should be addressed. Electronic mail: jorge.morales@ttu.edu. Tel.: (806) 742-3094. FAX: (806) 742-1289.

Unlike the previous approaches, direct-dynamics methods<sup>18</sup> can simulate chemical reactions without the cumbersome predetermination of complete PESs. With direct-dynamics methods, the potential energy and forces acting among the reactants are calculated “on the fly” as a simulation proceeds. Among several direct-dynamics methods,<sup>18</sup> the electron nuclear dynamics (END) theory<sup>19–21</sup> at its simplest level (SLEND) has proven feasible and accurate to simulate proton-molecule reactions. Developed by Deumens and Öhrn, END is a time-dependent, variational, non-adiabatic approach to direct dynamics that can incorporate different types of methodologies to describe nuclei and electrons simultaneously. Specifically, SLEND incorporates a classical-mechanics description for the nuclei and a single-determinantal wavefunction for the electrons. SLEND has been successfully applied to the simulation of various proton-molecule reactions, such as  $\text{H}^+ + \text{M}$ ,  $\text{M} = \text{H}_2$ ,<sup>14</sup>  $\text{CH}_4$ ,<sup>22</sup>  $\text{H}_2\text{O}$ ,<sup>23</sup>  $\text{C}_2\text{H}_2$ ,<sup>24,25</sup>  $\text{HF}$ ,<sup>26</sup>  $\text{CF}_4$ ,<sup>27</sup> etc. Of relevance to this investigation, a previous SLEND study of  $\text{H}^+ + \text{N}_2$  at  $E_{\text{Lab}} = 0.5, 1.5, \text{ and } 5.0$  keV (Ref. 28) predicted total and electron-transfer differential cross sections in good agreement with experimental data.<sup>28,29</sup> Those results certainly endorse this SLEND investigation that primarily focuses on an additional aspect of  $\text{H}^+ + \text{N}_2$ : its vibrational behavior at  $E_{\text{Lab}} = 30$  eV.

Given its suitability to simulate proton-molecule reactions without predetermined PESs, SLEND is herein applied to  $\text{H}^+ + \text{N}_2$  at  $E_{\text{Lab}} = 30$  eV with the Krutein and Linder experiment as a main standard for comparison. An important component in this investigation is a canonical coherent-states (CS) (Ref. 30) procedure to reconstruct vibrational state-to-state properties from the SLEND classical mechanics.<sup>14,31</sup> With a precedent set by the distribution of exact classical energy transfer (DECENT) method of Giese and Gentry,<sup>32</sup> the SLEND canonical CS procedure was originally formulated and successfully applied to the calculation of differential and integral cross sections of  $\text{H}^+ + \text{H}_2$  ( $v_i = 0$ )  $\rightarrow$   $\text{H}^+ + \text{H}_2$  ( $v_f = 0 - 6$ ) at  $E_{\text{Lab}} = 30$  eV.<sup>1,14</sup> The present investigation proves that the SLEND method involving computationally feasible approximations (nuclear classical mechanics, electronic single-determinantal wavefunction, CS reconstruction of vibrational state-to-state properties) provides results in good agreement with the experimental data. Furthermore, these SLEND results exhibit a level of accuracy comparable to that of the VCC-RIOS and QCT results obtained with higher computational effort (elaborate MRDCI PESs in both methods, costly quantum nuclear treatment in VCC-RIOS). In addition, this investigation provides a more complete chemical picture of  $\text{H}^+ + \text{N}_2$  at  $E_{\text{Lab}} = 30$  eV by investigating some details not scrutinized by the other two theoretical studies (e.g., prediction of reaction products, time-dependent evolution of the electron density, etc.).

The present investigation is organized as follows. In Sec. II, we explain the SLEND theory and its intrinsic CS procedure to reconstruct vibrational state-to-state properties; in Sec. III, we present computational details of the performed simulations; in Sec. IV, we report and discuss the SLEND results for  $\text{H}^+ + \text{N}_2$  at  $E_{\text{Lab}} = 30$  eV in comparison with

other theoretical and experimental results; finally, in Sec. V, we present some concluding remarks.

## II. THEORETICAL BACKGROUND

### A. The SLEND theory

Complete reviews of the END theory and its various realizations are given in Refs. 19–21. Therefore, only a brief outline of SLEND is presented here. Every END realization adopts a trial total wavefunction that is treated under the time-dependent variational principle (TDVP) (Ref. 33) to obtain dynamical equations. In SLEND, the trial total wavefunction  $|\Psi_{\text{SLEND}}(t)\rangle$  for a system with  $N_N$  nuclei and  $N_e$  electrons is the product of a nuclear  $|\mathbf{R}(t), \mathbf{P}(t)\rangle$  and an electronic  $|\mathbf{z}(t), \mathbf{R}(t)\rangle$  wavefunction:  $|\Psi_{\text{SLEND}}(t)\rangle = |\mathbf{R}(t), \mathbf{P}(t)\rangle |\mathbf{z}(t), \mathbf{R}(t)\rangle$ .  $|\mathbf{R}(t), \mathbf{P}(t)\rangle$  is a product of  $3N_N$  1D, frozen, narrow, Gaussian wave packets:

$$\begin{aligned} \langle \mathbf{X} | \mathbf{R}(t), \mathbf{P}(t) \rangle &= \prod_{i=1}^{3N_N} \langle X_i | R_i(t), P_i(t) \rangle \\ &= \prod_{i=1}^{3N_N} \exp \left\{ - \left( \frac{X_i - R_i(t)}{2\Delta R_i} \right)^2 \right. \\ &\quad \left. + i P_i(t) [X_i - R_i(t)] \right\}, \end{aligned} \quad (1)$$

with average positions  $\{R_i(t)\}$ , average momenta  $\{P_i(t)\}$ , and widths  $\{\Delta R_i\}$ ; those positions and momenta are the variational parameters of  $|\mathbf{R}(t), \mathbf{P}(t)\rangle$ . In practice,  $|\mathbf{R}(t), \mathbf{P}(t)\rangle$  is employed in the zero-width limit:  $\Delta R_i \rightarrow 0 \forall i$ , which renders a nuclear classical dynamics in terms of the conjugate variables  $\{R_i(t), P_i(t)\}$ .<sup>19–21,34</sup>  $|\mathbf{z}(t), \mathbf{R}(t)\rangle$  is a single-determinantal state in the Thouless representation.<sup>35</sup> Taking  $N_e$  occupied  $\{\psi_h\}$ , and  $K - N_e$  virtual  $\{\psi_p\}$  molecular spin-orbitals (MSOs), the Thouless single-determinantal state  $|\mathbf{z}(t), \mathbf{R}(t)\rangle$  from a reference state  $|0\rangle = |\psi_{N_e} \dots \psi_1\rangle$  is<sup>19,35</sup>

$$|\mathbf{z}(t), \mathbf{R}(t)\rangle = \exp \left( \sum_{p=N_e+1}^K \sum_{h=1}^{N_e} z_{ph}(t) b_p^\dagger b_h \right) |0\rangle, \quad (2)$$

$$\langle \mathbf{x} | \mathbf{z}(t), \mathbf{R}(t) \rangle = \det \{ \chi_h [\mathbf{x}_h; \mathbf{z}(t), \mathbf{R}(t)] \},$$

where  $\{\chi_h\}$  are the dynamical spin-orbitals (DSOs),<sup>19</sup>

$$\begin{aligned} \chi_h [\mathbf{x}; \mathbf{z}(t), \mathbf{R}(t)] &= \psi_h [\mathbf{x}; \mathbf{R}(t)] \\ &\quad + \sum_{p=N_e+1}^K \psi_p [\mathbf{x}; \mathbf{R}(t)] z_{ph} \quad (1 \leq h \leq N_e), \end{aligned} \quad (3)$$

whose molecular orbital coefficients are the complex-valued Thouless parameters  $\{z_{ph}(t)\}$ . The Thouless parameters, acting in pairs of generalized conjugate variables  $\{z_{ph}(t), z_{ph}^*(t)\}$ ,<sup>19,33</sup> and the nuclear wave packets' positions  $\{R_i(t)\}$  are the variational parameters of  $|\mathbf{z}(t), \mathbf{R}(t)\rangle$ . The MSOs are obtained at the time-independent unrestricted Hartree-Fock (UHF) level employing atomic basis set functions placed on the nuclear wave packets' centers  $\{R_i(t)\}$ . For that reason, the MSOs, DSOs, and  $|\mathbf{z}(t), \mathbf{R}(t)\rangle$  all depend on

$\{R_i(t)\}$ . Like the MSOs, the DSOs are spin-unrestricted so that the unrestricted determinant  $|\mathbf{z}(t), \mathbf{R}(t)\rangle$  can adequately describe bond-breaking and bond-forming processes. Unlike the MSOs, the DSOs are not orthogonal within spin blocks [cf. Eq. (3)]. Additionally, each DSO in  $|\mathbf{z}(t), \mathbf{R}(t)\rangle$  is a linear combination of one occupied MSO and all the virtual MSOs [cf. Eq. (3)]. Therefore,  $|\mathbf{z}(t), \mathbf{R}(t)\rangle$  does not necessarily remain on the ground state during evolution but can access the excited states. Hence, SLEND is a non-adiabatic method, quite in contrast with the QCT (Ref. 16) and VCC-RIOS (Ref. 17) methods, which only employ ground-state PESs. The advantages of employing a non-standard Thouless single-determinantal state in SLEND are discussed in full detail in Ref. 19. It suffices to explain herein that the Thouless representation provides a continuous and non-redundant parameterization of a general single-determinantal state  $|\mathbf{z}(t), \mathbf{R}(t)\rangle$  out of the reference  $|0\rangle$ ; such a parameterization is numerically advantageous for TDVP treatments.

The SLEND dynamical equations are obtained by subjecting the SLEND trial total wavefunction  $|\Psi_{SLEND}(t)\rangle$  to the TDVP.<sup>19-21</sup> That procedure implies the construction of the quantum Lagrangian  $L_{SLEND}$

$$L_{SLEND}[\Psi_{SLEND}, \Psi_{SLEND}^*] = \langle \Psi_{SLEND} | i \frac{\partial}{\partial t} - \hat{H}_{Total} | \Psi_{SLEND} \rangle \times \langle \Psi_{SLEND} | \Psi_{SLEND} \rangle^{-1}, \quad (4)$$

with the total Hamiltonian  $\hat{H}_{Total}$ , and imposing the stationary condition to its associated quantum action  $A_{SLEND}$ :  $\delta A_{SLEND}[\Psi_{SLEND}, \Psi_{SLEND}^*] = \delta \int_{t_1}^{t_2} dt L_{SLEND}[\Psi_{SLEND}, \Psi_{SLEND}^*] = 0$  with respect to the variational parameters:  $\{R_i(t), P_i(t), z_{ph}(t), z_{ph}^*(t)\}$  and with the boundary conditions:  $\delta |\Psi_{SLEND}(t_1)\rangle = \delta |\Psi_{SLEND}(t_2)\rangle = 0$ . In the zero-width limit of the nuclear wave packets ( $\Delta R_i \rightarrow 0 \forall i$ ), the mentioned procedure renders the SLEND dynamical equations for the variational parameters,<sup>19-21</sup>

$$\begin{bmatrix} iC & \mathbf{0} & iC_R & \mathbf{0} \\ \mathbf{0} & -iC^* & -iC_R^* & \mathbf{0} \\ iC_R^\dagger & -iC_R^T & C_{RR} & -\mathbf{I} \\ \mathbf{0} & \mathbf{0} & \mathbf{I} & \mathbf{0} \end{bmatrix} \begin{bmatrix} \frac{d\mathbf{z}}{dt} \\ \frac{d\mathbf{z}^*}{dt} \\ \frac{d\mathbf{R}}{dt} \\ \frac{d\mathbf{P}}{dt} \end{bmatrix} = \begin{bmatrix} \frac{\partial E_{Total}}{\partial \mathbf{z}^*} \\ \frac{\partial E_{Total}}{\partial \mathbf{z}} \\ \frac{\partial E_{Total}}{\partial \mathbf{R}} \\ \frac{\partial E_{Total}}{\partial \mathbf{P}} \end{bmatrix}, \quad (5)$$

with total energy  $E_{Total} = \sum_{i=1}^{N_N} \mathbf{P}_i^2 / 2M_i + \sum_{i=1, j>i}^{N_N} Z_i Z_j |\mathbf{R}_i - \mathbf{R}_j|^{-1} + \langle \mathbf{z}(t), \mathbf{R}(t) | \hat{H}_e | \mathbf{z}(t), \mathbf{R}(t) \rangle \langle \mathbf{z}(t), \mathbf{R}(t) | \mathbf{z}(t), \mathbf{R}(t) \rangle^{-1}$ , and dynamic metric matrices

$$\begin{aligned} (C_{XY})_{ik,jl} &= -2\text{Im} \frac{\partial^2 \ln S}{\partial X_{ik} \partial Y_{jl}} \Big|_{\mathbf{R}'=\mathbf{R}}; \\ (C_{X_{ik}})_{ph} &= \frac{\partial^2 \ln S}{\partial z_{ph}^* \partial X_{ik}} \Big|_{\mathbf{R}'=\mathbf{R}}; \\ C_{ph,qg} &= \frac{\partial^2 \ln S}{\partial z_{ph}^* \partial z_{qg}} \Big|_{\mathbf{R}'=\mathbf{R}}, \end{aligned} \quad (6)$$

where  $S = \langle \mathbf{z}(t), \mathbf{R}(t) | \mathbf{z}(t), \mathbf{R}(t) \rangle$ ;  $C_R$  and  $C_{RR}$  are the SLEND non-adiabatic coupling terms. The SLEND dynamical

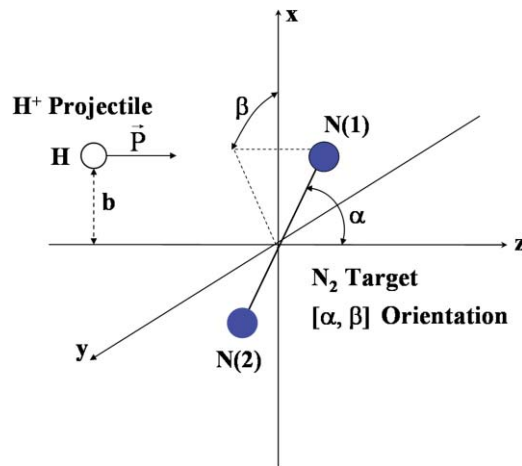


FIG. 1.  $H^+ + N_2$  reactants initial conditions; the spheres represent the classical nuclei with projectile impact parameter  $b$  and target orientation  $[\alpha, \beta]$ .

ical Eqs. (5) and (6) are a quantum generalization of the classical Hamilton equations in symplectic notation<sup>33,34</sup> and express the coupled nuclear and electronic dynamics in terms of the pairs of conjugate variables:  $\{R_i(t), P_i(t)\}$  and  $\{z_{ph}(t), z_{ph}^*(t)\}$ , respectively. In a SLEND simulation, reactants are prepared in an initial electronic state  $|\mathbf{z}^{(i)}, \mathbf{R}^{(i)}\rangle$  with initial positions and momenta  $\{R_i^{(i)}\}$  and  $\{P_i^{(i)}\}$  (cf. Fig. 1) that determine the initial SLEND wavefunction  $|\Psi_{SLEND}^{(i)}\rangle$ . The initial Thouless parameters can be taken as  $\mathbf{z}^{(i)} = \mathbf{0}$  so that  $|\mathbf{z}^{(i)} = \mathbf{0}, \mathbf{R}^{(i)} = |0\rangle$ , i.e., a UHF single-determinantal state corresponding to the reactants' super-molecule. At the end of a simulation, the final parameters  $\{R_i^{(f)}, P_i^{(f)}, z_{ph}^{(f)}, \text{ and } z_{ph}^{(f)*}\}$  obtained from Eqs. (5) and (6) determine the final SLEND wavefunction  $|\Psi_{SLEND}^{(f)}\rangle$  from which several dynamical properties can be calculated.

## B. Coherent-states reconstruction of state-to-state properties

The zero-width limit of the nuclear Gaussian wave packets  $|R_i(t), P_i(t)\rangle$ , Eq. (1), transforms them into Dirac delta functions that lack the quantum features of their finite-width originators. That limit generates the SLEND nuclear classical dynamics that has no discernible connection to the vibrational state-to-state properties of  $H^+ + N_2$ . Nonetheless, a procedure involving the canonical CS set<sup>30</sup> can accurately reconstruct those properties from SLEND.<sup>14,31</sup> Basically, that procedure reconstructs the narrow, finite-width wave packets that would correspond to a SLEND nuclear classical dynamics and calculates from those wave packets vibrational state-to-state properties by applying the canonical CS set. An outline of that CS procedure is given below, while more detailed accounts can be found in Refs. 14, 31, and 36.

In a Hilbert space, states  $\{|\zeta_i\rangle\}$  depending on a parameter set  $\{\zeta_i\}$  classify as CS if they satisfy two properties:<sup>30</sup> (I) The states  $\{|\zeta_i\rangle\}$  are continuous with respect to the parameters  $\{\zeta_i\}$ ; and (II) the states  $\{|\zeta_i\rangle\}$  achieve resolution of unity with a positive measure  $d\mu(\zeta_i)$ :  $\int d\mu(\zeta_i) |\zeta_i\rangle \langle \zeta_i| = \hat{1}$ . END has a close relationship with the CS theory since various types of CS sets have been employed in its realizations.<sup>19,21,37</sup> In SLEND,

two types of CS sets are employed.<sup>19</sup> First, each 1D Gaussian wave packet  $\{|R_i, P_i\rangle\}$  of  $|\mathbf{R}(t), \mathbf{P}(t)\rangle$ , Eq. (1), is a member of the canonical CS set with real parameters  $\{\zeta_i\} = \{R_i, P_i\}$ .<sup>30</sup> Second, the Thouless single-determinantal state  $|\mathbf{z}, \mathbf{R}\rangle$ , Eq. (2), is a member of the Thouless CS set<sup>30</sup> with complex parameters  $\{\zeta_i\} = \{z_{ph}\}$ . The original role of those CS sets was to represent the SLEND total trial wavefunction  $|\Psi_{\text{SLEND}}(t)\rangle$  and supply their CS parameters as adequate variational parameters for the TDVP treatment.<sup>19,33</sup> However, the canonical CS set  $\{|R_i, P_i\rangle\}$  plays an additional role in the nuclear vibrational description due to its association with the quantum harmonic oscillator.<sup>30</sup> Having a 1D harmonic-oscillator Hamiltonian  $\hat{H}_{HO}$  with mass  $m_i$ , angular frequency  $\omega_i$ , and eigenstates  $|v\rangle$  ( $v = 0, 1, 2, \dots$ ), the normalized canonical CS  $\{|R_i, P_i\rangle\}$  are<sup>30</sup>

$$\begin{aligned} |R_i, P_i\rangle &= |Z_i\rangle \\ &= \exp\left(-\frac{1}{2}|Z_i|^2\right) \sum_{v=0}^{\infty} \frac{Z_i^v}{\sqrt{v!}} |v\rangle, \quad (v = 0, 1, \dots), \\ Z_i &= \sqrt{m_i\omega_i/2}R_i + i\sqrt{1/2m_i\omega_i}P_i, \quad (i = 1, \dots, 3N_N), \\ \langle X_i | R_i, P_i\rangle &= \left(\frac{m_i\omega_i}{\pi}\right)^{1/4} \\ &\quad \times \exp\left[-\left(\frac{X_i - R_i}{2\Delta R_i}\right)^2 + iP_i(X_i - R_i)\right], \end{aligned} \quad (7)$$

where  $\Delta R_i = \sqrt{1/2m_i\omega_i}$  and the alternative complex parameter  $Z_i$  comprises the two real parameters  $R_i$  and  $P_i$ . Equation (7) provides a resolution of a SLEND 1D nuclear wave packet into the eigenstates  $|v\rangle$ . When evolving with  $\hat{H}_{HO}$ , a canonical CS preserves its form without spreading/squeezing<sup>38</sup> and exhibits quasiclassical behavior.<sup>38</sup> In a CS context, the latter means that the CS average positions  $\langle R_i, P_i | \hat{X}_i | R_i, P_i\rangle = R_i$ , and momenta  $\langle R_i, P_i | \hat{P}_i | R_i, P_i\rangle = P_i$  evolve with  $\hat{H}_{HO}$  just as the positions and momenta of its classical-mechanics counterpart does with the Hamiltonian  $H_{HO}(R_i, P_i)$ . The same behaviors occur under the TDVP. The previous properties allow the reconstruction of quantum vibrational features from the SLEND nuclear classical dynamics. For instance, if a diatomic molecule AB is SLEND-simulated in a vibrational motion, a canonical CS,  $|Z_{\text{AB}}(t)\rangle$ ,  $Z_{\text{AB}}(t) = \sqrt{m_{\text{AB}}\omega_{\text{AB}}/2}R_{\text{AB}}(t) + i\sqrt{1/2m_{\text{AB}}\omega_{\text{AB}}}P_{\text{AB}}(t)$ , can be reconstructed with AB's effective mass  $m_{\text{AB}}$  and vibrational angular frequency  $\omega_{\text{AB}}$  so that its quasiclassical vibration replicates the SLEND classical vibration.<sup>14,31</sup> Then, from Eq. (7), the probability to find the SLEND-simulated molecule AB in the eigenstate  $|v\rangle$  is a Poisson distribution  $P_v$ :

$$\begin{aligned} P_v &= \exp(-|Z_{\text{AB}}|^2) \frac{|Z_{\text{AB}}|^{2v}}{v!} \\ &= \exp(-E_{\text{Vib}}^{\text{AB}}/\omega_{\text{AB}}) \frac{(E_{\text{Vib}}^{\text{AB}}/\omega_{\text{AB}})^v}{v!}, \\ E_{\text{Vib}}^{\text{AB}} &= \omega_{\text{AB}} |Z_{\text{AB}}|^2 = \frac{1}{2m_{\text{AB}}}P_{\text{AB}}^2 + \frac{1}{2}m_{\text{AB}}\omega_{\text{AB}}^2 R_{\text{AB}}^2, \end{aligned} \quad (8)$$

where  $E_{\text{Vib}}^{\text{AB}}$  is the SLEND classical vibrational energy of molecule AB.

In a  $\text{H}^+ + \text{AB}$  collision, the CS quantum reconstruction procedure needs to be applied to AB only at initial and final times to resolve dynamical properties into the initial and final vibrational eigenstates of AB.<sup>14,31,36</sup> At those times,  $\text{H}^+$  and AB are so separated that AB can be considered as an isolated molecule. However, the actual application of the CS procedure to an isolated AB is more involved than that of the above example, because that molecule may not be in a single vibrational motion but in a combination of translational and rovibrational motions.<sup>14,31,36</sup> At initial and final times, the AB nuclear wavefunction  $|\Psi_{\text{N}}^{\text{AB}}\rangle$  of its total wavefunction  $|\Psi_{\text{SLEND}}^{\text{AB}}\rangle = |\Psi_{\text{N}}^{\text{AB}}\rangle|\Psi_{\text{e}}^{\text{AB}}\rangle$  can be reconstructed with finite widths  $\Delta R_i$  so that their positions and momenta match those of the SLEND nuclear classical dynamics. By changing from the variables  $\{R_i, P_i\}$  to those of the AB center of mass and the internal ones, assuming harmonic vibrations, and adopting the rigid-rotor approximation<sup>39</sup> of spectroscopy to separate rotational and vibrational motions,  $|\Psi_{\text{SLEND}}^{\text{AB}}\rangle$  and its total energy  $E_{\text{Total}}^{\text{AB}}$  become<sup>31,36</sup>  $|\Psi_{\text{SLEND}}^{\text{AB}}\rangle = |\Psi_{\text{Trans}}^{\text{AB}}\rangle|\Psi_{\text{Rot}}^{\text{AB}}\rangle|\Psi_{\text{Vib}}^{\text{AB}}\rangle|\Psi_{\text{e}}^{\text{AB}}\rangle$  and  $E_{\text{Total}}^{\text{AB}} = E_{\text{Trans}}^{\text{AB}} + E_{\text{Rot}}^{\text{AB}} + E_{\text{Vib}}^{\text{AB}} + E_{\text{e}}^{\text{AB eq}}$ , respectively, where all separations are exact, except for that between rotational and vibrational motions.<sup>31,36</sup>  $|\Psi_{\text{Trans}}^{\text{AB}}\rangle$  is a 3D wave packet describing the center-of-mass translational motion,  $|\Psi_{\text{Rot}}^{\text{AB}}\rangle$  is a wavefunction describing the AB rotation,<sup>31,36</sup> and  $|\Psi_{\text{Vib}}^{\text{AB}}\rangle$  is a canonical CS describing quasiclassically the AB vibration.  $E_{\text{Trans}}^{\text{AB}}$  is AB center-of-mass translational energy,  $E_{\text{e}}^{\text{AB eq}}$  is AB total electronic energy at its equilibrium bond distance  $R_{\text{AB eq}}$ , and  $E_{\text{Rot}}^{\text{AB}} = L_{\text{AB}}^2/2m_{\text{AB}}R_{\text{AB eq}}^2$  is the estimated AB rotational energy as a rigid rotor of length  $R_{\text{AB eq}}$ , where  $L_{\text{AB}}$  and  $m_{\text{AB}}$  are AB total angular momentum and effective mass, respectively.<sup>31,36</sup> Therefore, the vibrational energy  $E_{\text{Vib}}^{\text{AB}}$  associated with the canonical CS  $|\Psi_{\text{Vib}}^{\text{AB}}\rangle$  is estimated as  $E_{\text{Vib}}^{\text{AB}} = E_{\text{Total}}^{\text{AB}} - E_{\text{Trans}}^{\text{AB}} - E_{\text{Rot}}^{\text{AB}} - E_{\text{e}}^{\text{AB eq}}$ , where the last four terms are readily obtained from a SLEND simulation.  $E_{\text{Vib}}^{\text{AB}}$  is then used in Eq. (8) to resolve  $|\Psi_{\text{Vib}}^{\text{AB}}\rangle$  and pertinent dynamical properties into the AB vibrational eigenstates  $|v\rangle$  (See Sec. IV C).

The described canonical CS procedure assumes that the AB molecule exhibits harmonic behavior; however, that procedure also works well with molecules having a moderate departure from harmonic behavior (e.g.,  $\text{H}_2$  in Ref. 14 and  $\text{N}_2$  as shown in Sec. IV C below). The canonical CS procedure for a diatomic molecule can be readily generalized to each of the vibrational normal modes of a polyatomic molecule. An analogous procedure to reconstruct quantum rotational properties via a rotational CS is discussed in Ref. 36. That rotational CS will be used to calculate rotational transitional probabilities in  $\text{H}^+ + \text{N}_2$  and other systems in the near future. The Thouless CS set should describe the quantum electronic dynamics, and therefore it does not exhibit a quasiclassical behavior with the electronic Hamiltonian. Nonetheless, a quasiclassical CS set for electrons has been proposed in the context of quantum/classical methods.<sup>40</sup>

### III. COMPUTATIONAL DETAILS

Present SLEND calculations are conducted with our program CSDYN 1.0 (A. Perera, T. V. Grimes, and J. A.

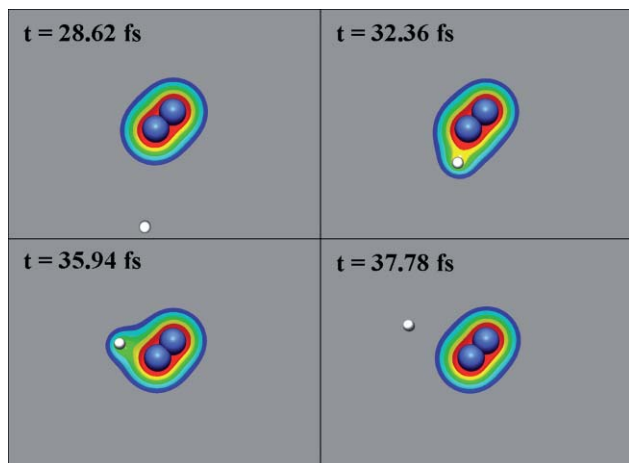


FIG. 2. Four sequential snapshots of a SLEND/6-31G\*\* simulation of  $\text{H}^+ + \text{N}_2$  at  $E_{\text{Lab}} = 30$  eV from target orientation  $[135^\circ, 0^\circ]$  and  $b = 1.6$  a.u. Time is given in femtoseconds. The spheres represent the nuclei (blue spheres = N, white sphere = H) and the colored clouds, electron density isosurfaces that increase in value through the sequence: blue, cyan, green, yellow, and red. The snapshots show non-charge-transfer scattering, Eq. (9).

Morales, CSDYN 1.0, Texas Tech University, Lubbock, Texas, 2008-2010), developed from the ENDYNE 2.7 and 2.8 programs (E. Deumens *et al.*, ENDYNE: *Electron Nuclear Dynamics Simulations*, Version 2 Release 8, Quantum Theory Project, University of Florida, 1997). Distinct features of CSDYN 1.0 include: a novel END/Kohn-Sham (KS) density-functional-theory (DFT) method (END/KSDFT),<sup>41</sup> effective core potential implementations in SLEND and END/KSDFT, auxiliary codes to calculate dynamical properties, and visualization tools to prepare animations of the simulated reactions (cf. Fig. 2).

Present SLEND calculations use three atomic basis sets: 6-31G\*\*, 6-31G, and STO-3G. 6-31G\*\* is the routine middle-size basis set for time-independent electronic structure calculations and is taken as such for the present time-dependent calculations. Comparison of SLEND/6-31G\*\* and SLEND/6-31G simulations aims at determining the effect of polarization functions on the results; overall, that effect turns out to be moderate although SLEND/6-31G\*\* proves more accurate than SLEND/6-31G as shown below. SLEND/STO-3G simulations aim at determining the quality of dynamics with a minimal basis set. Although SLEND/STO-3G satisfactorily predicted some dynamical properties of  $\text{H}^+ + \text{CH}_4$ ,<sup>22</sup>  $\text{H}^+ + \text{C}_2\text{H}_2$ ,<sup>25</sup> at  $E_{\text{Lab}} = 30$  eV and  $\text{H}^+ + \text{H}_2\text{O}$ ,<sup>23</sup> at  $E_{\text{Lab}} = 49$  eV, that is not the case with some properties of the present system as discussed below. As is known in time-independent electronic structure theory,<sup>39</sup> 6-31G and 6-31G\*\* render better electronic and structural Hartree-Fock properties for  $\text{N}_2$  than STO-3G (e.g., better ionization energies and better bond distances). However, the effect of those basis sets on the dynamics of this system is investigated herein for the first time.

The initial nuclear variables  $\{R_i(t), P_i(t)\}$  for the reactants  $\text{H}^+$  and  $\text{N}_2$  in the present simulations are shown in Fig. 1. The nuclei initially forming the target  $\text{N}_2$  are labeled N(1) and N(2), respectively, and the nucleus of the incoming  $\text{H}^+$  projectile is labeled H. The initial target  $\text{N}_2$  is in its

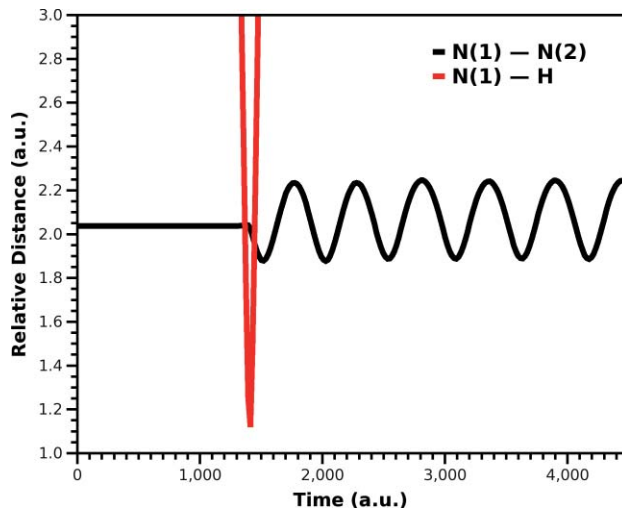


FIG. 3. Nuclear relative distance vs. time of a SLEND/6-31G\*\* simulation of  $\text{H}^+ + \text{N}_2$  at  $E_{\text{Lab}} = 30$  eV from orientation  $[135^\circ, 0^\circ]$  and  $b = 1.6$  a.u., a non-charge-transfer scattering, Eq. (9). The N(1)-H relative distance indicates that the reactants' closest approach occurs at  $\sim 1405$  a.u. ( $= 33.98$  fs.). The N(1)-N(2) relative distance indicates that  $\text{N}_2$  remains bonded and oscillating after that closest approach.

UHF electronic ground state and equilibrium geometry, at rest ( $\mathbf{P}_{\text{N}(1)}^{(i)} = \mathbf{P}_{\text{N}(2)}^{(i)} = \mathbf{0}$ ), and with its center of mass at  $(0.0, 0.0, 0.0)$ . From the CS quantum reconstruction procedure, those initial conditions correspond to the  $\text{N}_2$  vibrational ground state  $|v_i = 0\rangle$ . The angular orientation  $[\alpha, \beta]$  of the initial target is determined by the angles  $\alpha$  ( $0^\circ \leq \alpha \leq 180^\circ$ ) and  $\beta$  ( $0^\circ \leq \beta \leq 360^\circ$ ) measured from the N(1) terminus (cf. Fig. 1). The  $\text{H}^+$  projectile is initially placed at  $(b, 0.0, -50.00$  a.u.), where  $b \geq 0$  is the impact parameter, and with initial momentum  $\mathbf{P}_{\text{H}^+}^{(i)} = (0.0, 0.0, +P_{\text{H}^+}^{(i)})$  corresponding to a kinetic energy  $E_{\text{Lab}} = P_{\text{H}^+}^{(i)2} / 2M_{\text{H}^+} = 30$  eV. The SLEND simulations start from a set of target orientations  $[\alpha, \beta]$  and projectile impact parameters  $b$ . By taking advantage of the  $D_{\infty h}$  symmetry of  $\text{N}_2$ , only angles in the ranges  $0^\circ \leq \alpha < 180^\circ$  and  $0^\circ \leq \beta \leq 90^\circ$  need to be considered in order to generate non-equivalent initial orientations. Within those ranges,  $\alpha$  and  $\beta$  are varied in steps of  $\Delta\alpha = 45^\circ$  and  $\Delta\beta = 45^\circ$ , which generates 9 non-equivalent initial orientations. For each of those orientations, the impact parameter  $b$  is varied in the range  $0.0 \leq b \leq 7.9$  a.u. in steps of  $\Delta b = 0.1$  a.u. Those initial conditions generate 720 individual simulations. Each simulation is run for a total time of 2900 a.u. ( $= 70.14$  fs), which allows a complete separation of the products. To check long-term behaviors, a few trajectories were run for a total time of 4500 a.u. ( $= 108.85$  fs; cf. Figs. 2 and 3). When a simulation is complete, its final state is analyzed to characterize the simulated process and calculate various dynamical properties.

## IV. RESULTS AND DISCUSSION

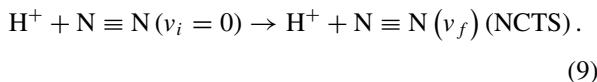
### A. Reactive processes and simulations analysis

Present SLEND simulations of  $\text{H}^+ + \text{N}_2$  at  $E_{\text{Lab}} = 30$  eV predict only two reactive processes, namely:

TABLE I. Collision processes from selected target orientations  $[\alpha, \beta]$  vs. impact parameter  $b$  and employed basis set (STO-3G, 6-31G, and 6-31G\*\*): NCTS, non-charge-transfer scattering, Eq. (9);  $N \equiv ND$ ,  $N_2$  collision-induced dissociation, Eq. (10).

$[\alpha, \beta]$	$b$ (a.u.)	Collision processes		
		STO-3G	6-31G	6-31G**
$[0^\circ, 0^\circ]$	0.0–0.2	$N \equiv ND$	NCTS	NCTS
	0.3–6.9	NCTS	NCTS	NCTS
$[45^\circ, 0^\circ]$	0.0–0.6	NCTS	NCTS	NCTS
	0.7–1.3	$N \equiv ND$	NCTS	NCTS
	1.4–6.9	NCTS	NCTS	NCTS
$[90^\circ, 0^\circ]$	0.0–0.2	$N \equiv ND$	$N \equiv ND$	NCTS
	0.3–0.7	$N \equiv ND$	NCTS	NCTS
	0.7–6.9	NCTS	NCTS	NCTS
$[135^\circ, 0^\circ]$	0.0–6.9	NCTS	NCTS	NCTS

- Non-charge-transfer scattering (NCTS), where the  $H^+$  projectile is scattered off while exciting the vibrational degree of freedom of  $N_2$  and, in a much lesser extent, the rotational and electronic ones:



- Collision-induced  $N_2$  dissociation ( $N \equiv ND$ ):

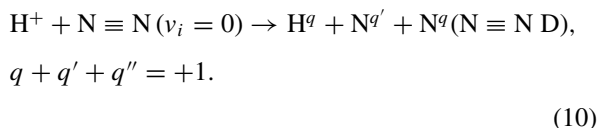


Table I lists those processes from selected target orientations as a function of the impact parameter  $b$  and employed basis sets. In the present simulations,  $N \equiv ND$  only occurs at a few small impact parameters  $b \leq 1.30$  a.u. SLEND/6-31G\*\* predicts no  $N \equiv ND$ . SLEND/STO-3G predicts considerably more  $N \equiv ND$  events than SLEND/6-31G, but this is likely an overestimation by that minimal basis set. In most SLEND simulations of  $H^+$ -molecule reactions,<sup>14,22,23,25</sup> a non-dissociative process is a combination of NCTS and charge-transfer scattering, each with a probability to happen. In the present simulations, the probability of the charge-transfer scattering  $H^+ + N_2 \rightarrow H + N_2^+$  is negligible; therefore, no significant charge-transfer reaction is predicted for  $H^+ + N_2$  at  $E_{Lab} = 30$  eV in agreement with experiments.<sup>2-5</sup> Similarly, the present simulations do not predict  $N_2H^+$  formation:  $H^+ + N_2 \rightarrow N_2H^+$ . Obviously, 30 eV is too high an energy to lead to a stable  $N_2H^+$ . Energies lower than 30 eV may lead to  $N_2H^+$  formation.

Figure 2 shows four sequential snapshots of a SLEND/6-31G\*\* simulation of  $H^+ + N_2$  at  $E_{Lab} = 30$  eV from orientation  $[135^\circ, 0^\circ]$  and  $b = 1.6$  a.u. that leads to a NCTS process. In Fig. 2, the spheres represent the nuclei (blue spheres = N, white sphere = H) and the colored clouds represent electron density isosurfaces that increase in value through the color sequence: blue, cyan, green, yellow, and red. In Fig. 2, the  $H^+$  projectile approaching  $N_2$  perturbs the latter's electron density. A temporary electron transfer from  $N_2$  to  $H^+$

occurs during their closest approach, but the projectile is finally scattered as  $H^+$  without gaining one electron. Figure 3 shows the  $N(1) - N(2)$  and  $N(1) - H$  relative distances vs. time for the same simulation of Fig. 2. After the time of the closest  $H^+ - N_2$  approach ( $\sim 1405$  a.u. = 33.98 fs.), the  $N(1) - N(2)$  relative distance indicates that  $N_2$  remains bonded and vibrating. The features shown in Figs. 2 and 3 (moderate vibrational excitation, slight rotational and electronic excitations, no charge transfer) are common to all the simulated NCTS. That considerable inertia of  $N_2$  during  $H^+$  collisions at  $E_{Lab} = 30$  eV is in agreement with experimental results.<sup>2-5</sup>

## B. Scattering patterns

The outgoing  $H^+$  scattering angle  $\theta_{Lab}(b)$  as a function of the impact parameter  $b$  is of particular interest because it provides details of the dynamics and takes part in the calculation of differential cross sections. From the initial conditions in Fig. 1, the outgoing  $H^+$  scattering angle  $\theta_{Lab}$  relative to the positive z-axis is

$$\sin \theta_{Lab} = \frac{\left(P_{H^+}^{(f)2} + P_{H^+}^{(f)2}\right)^{1/2}}{\left(P_{H^+}^{(f)2} + P_{H^+}^{(f)2} + P_{H^+}^{(f)2}\right)^{1/2}};$$

$$(0 \leq \theta_{Lab} \leq 180^\circ), \quad (11)$$

where  $\{P_{H^+}^{(f)}\}(i = x, y, z)$  are the  $H^+$  momentum components at final time.  $\theta_{Lab}(b)$  is related to the deflection function  $\Theta_{Lab}(b)$ :<sup>42</sup>  $\theta_{Lab}(b) = |\Theta_{Lab}(b)|$ , where  $\Theta_{Lab}(b) > 0$  ( $< 0$ ) for repulsive (attractive) scattering. Figure 4 shows representative plots of  $\theta_{Lab}(b)$  vs.  $b$  from the  $[90^\circ, 0^\circ]$  orientation for each basis set. As is usual in  $H^+$ -molecule collisions,<sup>14,22,23,25-27</sup>  $\theta_{Lab}(b)$  exhibits a forward glory scattering angle<sup>42</sup>  $\theta_{Lab}(b_{FG}) = 0^\circ$  (i.e., no deflection) at  $b = b_{FG}$  and a classical rainbow scattering angle<sup>42</sup>  $\theta_{Lab}(b_R) = \theta_{Lab}^{C.R.}$  at  $b = b_R > b_{FG}$  that is a maximum of  $\theta_{Lab}(b)$  (cf. Fig. 4).  $b_{FG}$  separates the repulsive ( $b < b_{FG}$ ) and attractive

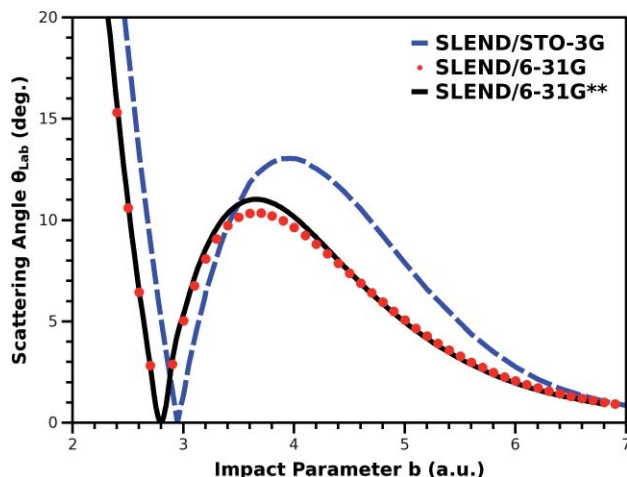


FIG. 4.  $H^+$  scattering angle  $\theta_{Lab}(b)$  vs. impact parameter  $b$  from  $[90^\circ, 0^\circ]$  orientation at the SLEND/STO-3G, /6-31G, and /6-31G\*\* levels. The maxima in  $\theta_{Lab}(b)$  are the classical rainbow scattering angles  $\theta_{Lab}^{C.R.}$ .

TABLE II. Classical  $\theta_{Lab}^{C.R.}$  and semi-classical  $\theta_{Lab}^{SC.R.}$  rainbow scattering angles from selected target orientations  $[\alpha, \beta]$ ; all values in deg. ( $^\circ$ ).

$[\alpha, \beta]$	SLEND/STO-3G		SLEND/6-31G		SLEND/6-31G**	
	$\theta_{Lab}^{C.R.}$	$\theta_{Lab}^{SC.R.}$	$\theta_{Lab}^{C.R.}$	$\theta_{Lab}^{SC.R.}$	$\theta_{Lab}^{C.R.}$	$\theta_{Lab}^{SC.R.}$
$[0^\circ, 0^\circ]$	18.3	16.0	12.5	10.4	14.1	11.8
$[45^\circ, 0^\circ]$	13.7	11.6	10.8	8.8	11.4	9.4
$[90^\circ, 0^\circ]$	13.1	11.1	10.4	8.5	11.0	9.1
$[135^\circ, 0^\circ]$	14.7	12.7	10.5	8.6	11.9	9.8

( $b > b_{FG}$ ) intervals of the projectile-target interaction;  $\theta_{Lab}^{C.R.}$  corresponds to the maximum attractive deflection of the projectile. Rainbow angle values are related to the parameters defining analytical projectile-target PESs;<sup>42</sup> therefore, an accurate prediction of a rainbow angle indicates a good description of the projectile-target interaction. The  $\theta_{Lab}^{C.R.}$  values from selected target orientations are listed in Table II along with their semi-classical counterparts  $\theta_{Lab}^{SC.R.}$ . The semi-classical rainbow angles are obtained from the semi-classical calculation of differential cross sections (see Sec. IV C). Closer to a quantum treatment,  $\theta_{Lab}^{SC.R.}$  values are more accurate than the  $\theta_{Lab}^{C.R.}$  ones and are therefore considered as the best rainbow angle prediction in this study. As shown in Table II, most  $\theta_{Lab}^{SC.R.}$  with SLEND/6-31G and /6-31G\*\* are close to the experimental rainbow angle  $\theta_{Lab}^{Expt.R.} = 9^\circ$ ,<sup>5</sup> which suggests a good description of the  $H^+ - N_2$  interaction by SLEND/6-31G and /6-31G\*\*. Moreover,  $\theta_{Lab}^{SC.R.}$  values with those basis sets differ moderately in the range:  $0.6^\circ < (\theta_{Lab}^{SC.R. 6-31G**} - \theta_{Lab}^{SC.R. 6-31G}) < 1.6^\circ$  over all the tested target orientations. This suggests that addition of polarization functions to a basis set has a moderate effect on the rainbow angle prediction. In contrast, values of  $\theta_{Lab}^{SC.R.}$  with SLEND/STO-3G do not agree well with the experimental rainbow angle. This indicates that the  $H^+ - N_2$  interaction computed with the STO-3G basis set in the SLEND framework are less accurate than those computed with the 6-31G and 6-31G\*\* basis sets.

### C. Vibrationally resolved properties and average vibrational energy transfer

Calculation of vibrationally resolved properties from SLEND simulations follows from the canonical CS procedure outlined in Sec. II B. That procedure assumes negligible anharmonicity in  $N_2$ . To test that condition, Table III lists the  $N_2$  vibrational energies for  $v = 0 - 2$  from the numerical solution of the nuclear Schrödinger equation at the Hartree-Fock(HF)/6-31G and /6-31G\*\* levels,  $E_v^{Num.}$ , and from the harmonic approximation,  $E_v^{Har.}$ . Table III also lists the same data for  $H_2$  at the HF/pVDZ level used in the SLEND study of  $H^+ + H_2 (v_i = 0) \rightarrow H^+ + H_2 (v_f = 0 - 6)$  at  $E_{Lab} = 30$  eV.<sup>14</sup> To estimate the degree of anharmonicity, Table III shows the relative differences  $|(E_v^{Num.} - E_{v-1}^{Num.}) - 2E_0^{Num.}| \times 100/2E_0^{Num.}$  per vibrational level  $v$ , which measure the relative deviation of the energy level separations  $E_v^{Num.} - E_{v-1}^{Num.}$  from the constant harmonic separation  $h\nu^{Num.} = 2E_0^{Num.}$ ; also given are the experimental and theoretical frequencies at the HF/6-31G and /6-31G\*\* levels

TABLE III.  $N_2$  and  $H_2$  vibrational energy levels calculated numerically at the Hartree-Fock (HF) level with different basis sets,  $E_v^{Num.}$ , and assuming harmonic separation,  $E_v^{Har.}$ . The  $H_2$  data were used in Ref. 14. Values of  $|(E_v^{Num.} - E_{v-1}^{Num.}) - 2E_0^{Num.}| \times 100/2E_0^{Num.}$  are given between parentheses to estimate anharmonicity (see text). Experimental (NIST data set) and calculated (harmonic approximation) frequencies of  $N_2$  are also listed. All values are in  $cm^{-1}$ .

Vibrational level	$N_2$		$H_2$	
	$E_v^{Num.}$ 6-31G**	$E_v^{Har.}$	$E_v^{Num.}$ PVDZ	$E_v^{Har.}$
$v = 0$	1374.4	1374.4	2238.7	2238.7
1	4086.2 (1.35)	4123.2	6615.6 (2.24)	6716.1
2	6691.6 (5.22)	6872.0	10773.8 (7.13)	11193.5
Vibrational level	$E_v^{Num.}$ 6-31G	$E_v^{Har.}$	$N_2$ Vibrational frequencies	
$v = 0$	1297.5	1297.5	Expt.:	2358.6
1	3750.1 (5.49)	3892.5	HF/6-31G**:	2758.0
2	5969.4 (14.5)	6487.5	HF/6-31G:	2662.2

within the harmonic approximation. Table III reveals that both  $N_2$  and  $H_2$  depart moderately from harmonic behavior for  $v = 0 - 2$  and that  $N_2$  at the HF/6-31G\*\* level is less anharmonic than  $H_2$  at the HF/pVDZ level. Since the canonical CS procedure proved accurate in  $H_2$  excitations with  $v_f = 0 - 6$ ,<sup>14</sup> it should be accurate in the low  $N_2$  excitations with  $v_f = 0 - 1$ , where anharmonic effects are less prominent. Results shown below corroborate that expectation.

The first vibrational property to be examined is the average vibrational energy transfer to  $N_2$  by  $H^+$  collision,  $\langle \Delta E_{Vib}(\theta_{Lab}) \rangle$ . In an individual SLEND simulation from impact parameter  $b$  and target orientation  $[\alpha, \beta]$ , the vibrational energy transfer to  $N_2$  by a  $H^+$  scattered to  $\theta_{Lab}(b; [\alpha, \beta])$  is  $\Delta E_{Vib}[\theta_{Lab}(b; [\alpha, \beta])] = E_{Vib}^{N_2(f)}(b, [\alpha, \beta]) - E_{Vib}^{N_2(i)}(b, [\alpha, \beta])$ , where the last two terms are the  $N_2$  vibrational energies at final and initial times, respectively (see Sec. II B for their evaluation).  $\langle \Delta E_{Vib}(\theta_{Lab}) \rangle$  is obtained by averaging the values of  $\Delta E_{Vib}[\theta_{Lab}(b; [\alpha, \beta])]$  from all the performed simulations (cf. Refs. 14 and 22). Figure 5 shows plots of  $\langle \Delta E_{Vib}(\theta_{Lab}) \rangle$  vs.  $\theta_{Lab}$  calculated at the SLEND/6-31-G\*\*, /6-31G, and /STO-3G levels along with the result from the Krutein and Linder experiment.<sup>5</sup> SLEND/6-31G\*\* and /6-31G  $\langle \Delta E_{Vib}(\theta_{Lab}) \rangle$  differ slightly from each other but both agree well with the experimental result. However, SLEND/STO-3G  $\langle \Delta E_{Vib}(\theta_{Lab}) \rangle$  differs considerably from the experimental result by as much as 190 meV. Such a discrepancy indicates that the SLEND/STO-3G description of the  $H^+ - N_2$  interaction is not accurate enough. In Fig. 6, the SLEND/6-31G\*\*  $\langle \Delta E_{Vib}(\theta_{Lab}) \rangle$  is compared with its counterparts from VCC-RIOS (Ref. 17) and QCT (Ref. 16) calculations and again with the experimental result. The SLEND/6-31G\*\* result is somewhat comparable to the QCT/PES II result.<sup>5</sup> Curiously, the entirely quantum-mechanical VCC-RIOS result departs farther from the experimental result than the SLEND/6-31G\*\* and QCT ones, despite the fact that the last two methods employ nuclear classical mechanics.

The Krutein and Linder experiment also reported proton energy loss spectra for  $v_f = 0 - 1$  at scattering angles  $\theta_{Lab} = 5^\circ$  and  $8^\circ$ .<sup>5</sup> The calculation of the energy loss spectrum

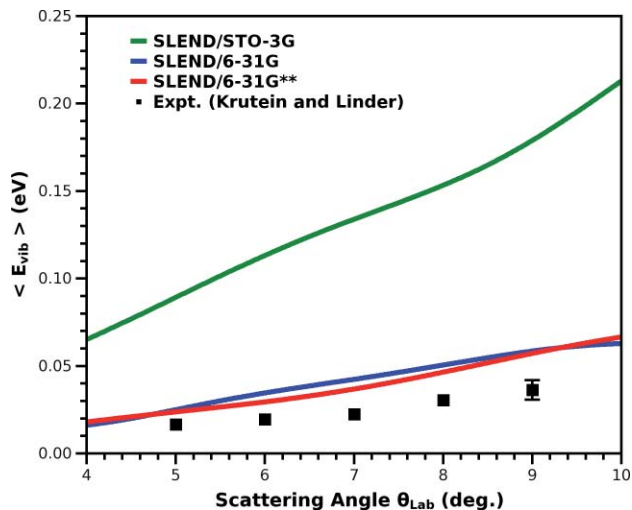


FIG. 5.  $N_2$  average vibrational energy transfer during collision. Results at the SLEND/STO-3G, /6-31G, and /6-31G\*\* levels are compared with the experimental result. (See Ref. 5).

with SLEND is similar to that of  $\langle \Delta E_{vib}(\theta_{Lab}) \rangle$  with the difference that the probability  $P_v[\theta_{Lab}(b; [\alpha, \beta])]$  to find the final  $N_2$  target in its vibrational eigenstate  $|v_f\rangle$  is now the sought property instead of  $\Delta E_{vib}[\theta_{Lab}(b; [\alpha, \beta])]$ . As explained in Sec. II B,  $P_v[\theta_{Lab}(b; [\alpha, \beta])]$  is the canonical CS Poisson distribution, Eq. (8), evaluated with the  $N_2$  final vibrational energy  $E_{Vib}^{N_2(f)}(b, [\alpha, \beta])$ . The proton energy spectrum is obtained by averaging the values of  $P_v[\theta_{Lab}(b; [\alpha, \beta])]$  from all the performed simulations. Figure 7 shows the SLEND/6-31G\*\* and /6-31G energy loss spectra along with the experimental results. The positions of the calculated peaks are slightly shifted from the experimental ones because the HF/6-31G\*\* and /6-31G vibrational energies differ slightly from their experimental counterparts. Inspection of the peak intensities in Fig. 7 shows that the SLEND/6-31G\*\* spectra compares well with the experimental results at  $\theta_{Lab} = 5^\circ$  and  $8^\circ$ .

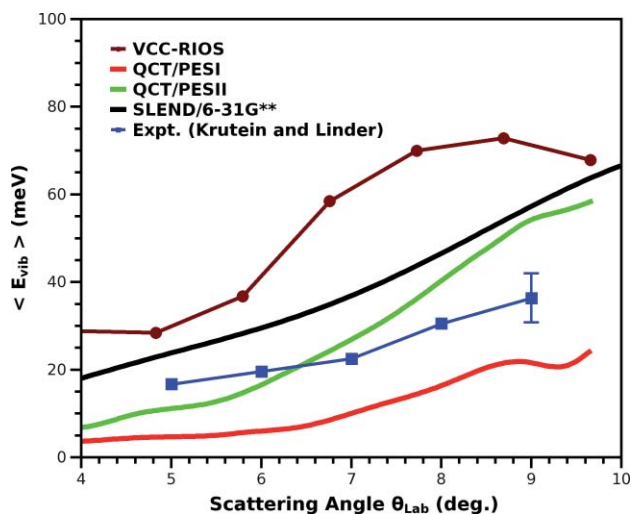


FIG. 6.  $N_2$  average vibrational energy transfer during collision. The result at the SLEND/6-31G\*\* level is compared with those from VCC-RIOS (see Ref. 17) and QCT (see Ref. 16) calculations and from an experiment. (see Ref. 5).

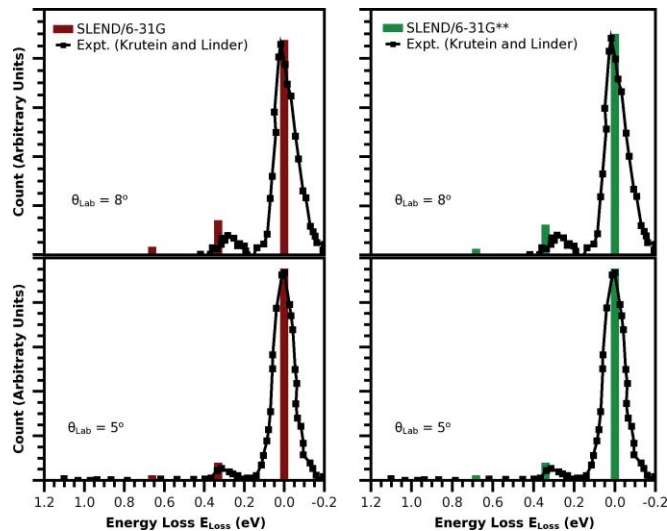


FIG. 7.  $H^+$  energy loss spectra computed at  $\theta_{Lab} = 5^\circ$  and  $8^\circ$ . Results at the SLEND/6-31G and /6-31G\*\* levels are compared with the experimental results. (See Ref. 5).

The SLEND/6-31G spectra also compare well at  $\theta_{Lab} = 5^\circ$ , but slightly overestimates the  $v = 1$  peak at  $\theta_{Lab} = 8^\circ$ ; that might result from the relatively higher anharmonicity of  $N_2$  at the HF/6-31G level than at the HF/6-31G\*\* one (cf. Table III). Since SLEND/6-31G\*\* provides better spectra, the vibrationally resolved differential cross sections will be calculated at that level below. The good spectrum prediction by SLEND/6-31G\*\* likely comes from two factors: first, the adequacy of the canonical CS Poisson distribution  $P_v[\theta_{Lab}(b; [\alpha, \beta])]$  with the moderately anharmonic  $N_2$  at  $v_f = 0-1$ , and second, the accuracy of the  $N_2$  final vibrational energy  $E_{Vib}^{N_2(f)}(b, [\alpha, \beta])$  as reflected by the SLEND/6-31G\*\*  $\langle \Delta E_{vib}(\theta_{Lab}) \rangle$  in Figs. 4 and 5;  $E_{Vib}^{N_2(f)}(b, [\alpha, \beta])$  is the critical input of  $P_v[\theta_{Lab}(b; [\alpha, \beta])]$ , Eq. (8). In contrast, SLEND/STO-3G values of  $E_{Vib}^{N_2(f)}(b, [\alpha, \beta])$  are far less accurate, as reflected by the SLEND/STO-3G  $\langle \Delta E_{vib}(\theta_{Lab}) \rangle$  in Fig. 4, so that the SLEND/STO-3G proton energy loss spectra and other vibrationally resolved properties are inaccurate.

The Krutein and Linder experiment also reported DCS for the  $H^+ + N_2(v_i = 0) \rightarrow H^+ + N_2(v_f = 0)$  channel.<sup>5</sup> As discussed in Refs. 14 and 26, DCS evaluations with SLEND involve adapting pertinent semi-classical expressions for DCS (Refs. 42 and 43) to the SLEND dynamics and the canonical CS quantum reconstruction procedure. The employed semi-classical formulae are evaluated in the center-of-mass frame ( $\theta_{c.m.}$ ), but the resulting DCS are transformed back to the laboratory frame ( $\theta_{Lab}$ ). A first approach to the vibrational state-to-state DCS  $d\sigma_{0 \rightarrow v_f}(\theta_{c.m.})/d\Omega|_{[\alpha, \beta]}$  for simulations from the orientation  $[\alpha, \beta]$  is obtained via the stationary phase approximation:<sup>26,42,43</sup>

$$\frac{d\sigma_{0 \rightarrow v_f}(\theta_{c.m.})}{d\Omega}|_{[\alpha, \beta]} = \left| \sum_{m=1}^N f_m^{[\alpha, \beta]}(\theta_{c.m.}) \right|^2;$$

$$f_m^{[\alpha, \beta]}(\theta_{c.m.}) = \left[ \frac{P_{v_f}(b_m) b_m}{\sin \theta_{c.m.} |d\Theta_{c.m.}(b)/db_m|} \right]^{1/2} \times \exp[i\delta(b_m)]|_{[\alpha, \beta]}, \quad (12)$$

where  $f_m^{[\alpha,\beta]}(\theta_{c.m.})$ ,  $P_{v_f}(b_m)$ , and  $\delta(b_m)$  are the scattering amplitude, canonical CS Poisson distribution, Eq. (8), and phase shift, respectively, from the  $N$  simulations whose  $H^+$ 's scatter in the direction  $\theta_{c.m.}$  ( $N = 3$  for  $\theta_{c.m.} < \theta_{c.m.}^{C.R.}$  and  $N = 1$  for  $\theta_{c.m.} > \theta_{c.m.}^{C.R.}$ );  $\delta(b_m)$  is obtained by integrating  $d\delta(b)/db = (k/2)\Theta_{c.m.}(b)$ ,<sup>42,43</sup> where  $k$  is the collision wavenumber. Equation (12) is accurate when  $\theta_{c.m.}$  is far from  $\theta_{c.m.}^{C.R.}$  but incorrectly predicts a steep drop in the DCS from the lit ( $\theta_{c.m.} < \theta_{c.m.}^{C.R.}$ ) to the dark ( $\theta_{c.m.} > \theta_{c.m.}^{C.R.}$ ) region and an unphysical classical rainbow singularity at  $\theta_{c.m.} = \theta_{c.m.}^{C.R.}$ .

$$f_{23}^{[\alpha,\beta]}(\theta_{c.m.}) = \begin{cases} \pi^{1/2} \exp\left[i\left(A_{23} - \frac{1}{4}\pi\right)\right] \left[B_+ \xi_{23}^{1/4} Ai(-\xi_{23}) - i B_- \xi_{23}^{-1/4} Ai'(-\xi_{23})\right] (\theta_{c.m.} < \theta_{c.m.}^{C.R.}) \\ \left(\frac{2\pi b_R}{k \sin(\theta_{c.m.})}\right)^{1/2} \frac{\exp\left\{i\left[2\delta(b_R) - k b_R \theta_{c.m.} - \frac{1}{4}\pi\right]\right\}}{|q_R|^{1/3}} Ai\left(\frac{\theta_{c.m.} - \theta_{c.m.}^{C.R.}}{|q_R|^{1/3}}\right) (\theta_{c.m.} \geq \theta_{c.m.}^{C.R.}) \end{cases}, \quad (13)$$

where  $Ai$  and  $Ai'$  are the Airy function and its first derivative,  $q_R = (1/2k^2)d^2\Theta_{c.m.}(b_R)/db^2$ ,  $B_{\pm}(\theta) = |f_2^{[\alpha,\beta]}(\theta_{c.m.})| \pm |f_3^{[\alpha,\beta]}(\theta_{c.m.})|$ ,  $A_{23}(\theta_{c.m.}) = 1/2[2\delta(b_3) + 2\delta(b_2) - k(b_3 + b_2)\theta_{c.m.}]$ , and  $\xi_{23}(\theta_{c.m.}) = \{3/4[2\delta(b_3) - 2\delta(b_2) - k(b_3 - b_2)\theta_{c.m.}]\}^{2/3}$ .  $f_{23}^{[\alpha,\beta]}(\theta_{c.m.})$  uses the uniform and the transitional Airy approximations in the lit and dark regions, respectively; both approximations become identical at  $\theta_{c.m.} = \theta_{c.m.}^{C.R.}$ . The combined use of Eqs. (12) and (13) provides very accurate DCS that do not display the above-mentioned problems near  $\theta_{c.m.}^{C.R.}$ . For instance, those DCS do not exhibit an unphysical singularity at  $\theta_{c.m.} = \theta_{c.m.}^{C.R.}$  but instead a bounded rainbow maximum at  $\theta_{c.m.} = \theta_{c.m.}^{SC.R.} < \theta_{c.m.}^{C.R.}$  that corresponds to the principal maximum of the Airy function.<sup>42</sup> Some  $\theta_{c.m.}^{SC.R.}$  values in the laboratory frame,  $\theta_{Lab}^{SC.R.}$ , were given in Table II.  $d\sigma_{0 \rightarrow v_f}(\theta_{c.m.})/d\Omega_{[\alpha,\beta]}$  is therefore calculated by combining Eqs. (12) and (13). The finally reported SLEND DCS involves transforming  $d\sigma_{0 \rightarrow v_f}(\theta_{c.m.})/d\Omega_{[\alpha,\beta]}$  to the laboratory frame and averaging them over all the target orientations  $[\alpha, \beta]$ .<sup>14,22,26</sup>

Figure 8 compares the DCS for the  $H^+ + N_2$  ( $v_i = 0$ )  $\rightarrow H^+ + N_2$  ( $v_f = 0$ ) channel from SLEND/6-31G\*\*, VCC-RIOS,<sup>17</sup> and QCT (Ref. 16) calculations and from the Krutein and Linder experiment.<sup>5</sup> The last three DCS, originally reported in arbitrary units, have been normalized to the absolute SLEND/6-31G\*\* DCS at the position of the experimental rainbow angle  $\theta_{Lab}^{Expt.R.} = 9^\circ$ .<sup>5</sup> The three theoretical DCS lie close to the experimental results. The VCC-RIOS DCS shows a rainbow angle maximum at  $\theta_{Lab} \approx 7^\circ$  that is  $2^\circ$  lower than the experimental one. The QCT DCS are calculated with a purely classical-mechanics expression, which can be obtained from Eq. (12) if its sum involving scattering amplitudes is performed incoherently and without the Airy approximations. Therefore, unlike the SLEND/6-31G\*\* DCS, the QCT DCS lacks the correction to the classical rainbow singularity and quantum oscillating patterns of the semi-classical theory. The QCT DCS were only reported for some discrete scattering angles; therefore, the QCT DCS does not show a clear rainbow

(the glory angle singularity<sup>42</sup> at  $\theta_{c.m.} = 0^\circ$  is irrelevant here because the experimental DCS are for  $\theta_{c.m.} \gg 0^\circ$  (Ref. 5)). Those problems can be solved by employing a combination of the uniform and transitional Airy approximations.<sup>42,43</sup> In that approach, the two scattering amplitudes in Eq. (12) corresponding to the two  $H^+$  trajectories whose coalescence causes the classical rainbow singularity (cf. Fig. 4), say  $f_2^{[\alpha,\beta]}(\theta_{c.m.})$  and  $f_3^{[\alpha,\beta]}(\theta_{c.m.})$ , are substituted by a single scattering amplitude  $f_{23}^{[\alpha,\beta]}(\theta_{c.m.})$ :

angle maximum but a shoulder between  $\theta_{Lab} = 10^\circ$  and  $12^\circ$  that must contain the classical rainbow angle singularity at an angle which is not plotted. Therefore, the predicted QCT rainbow angle is  $1^\circ$  to  $3^\circ$  larger than the experimental one. That overestimation is typical of a classical rainbow angle not corrected semi-classically (cf. Table II). The SLEND/6-31G\*\* DCS exhibits a rainbow angle maximum at  $\theta_{Lab} \approx 8.6^\circ$  that is only  $0.4^\circ$  smaller than the experimental one. The agreement of the SLEND/6-31G\*\* DCS for the inelastic channel with the experimental results is very good with regard to values, features, and rainbow angle prediction.

Finally, Fig. 9 compares the DCS for the  $H^+ + N_2$  ( $v_i = 0$ )  $\rightarrow H^+ + N_2$  ( $v_f = 1$ ) channel from SLEND/6-

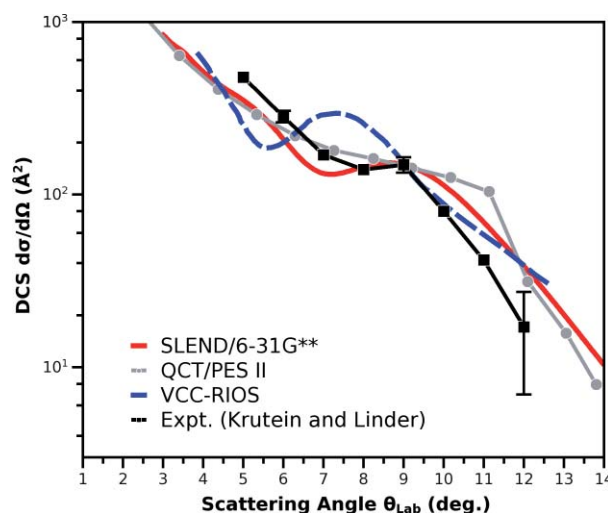


FIG. 8. Differential cross sections for the  $H^+ + N_2$  ( $v_i = 0$ )  $\rightarrow H^+ + N_2$  ( $v_f = 0$ ) elastic channel at  $E_{Lab} = 30$  eV vs. scattering angle: SLEND/6-31G\*\*, VCC-RIOS, (see Ref. 17) QCT, (see Ref. 16) and experimental (see Ref. 5) results. The last three results reported in arbitrary units are normalized to the absolute SLEND/6-31G\*\* DCS at the experimental rainbow angle  $\theta_{Lab}^{Expt.R.} = 9^\circ$ .

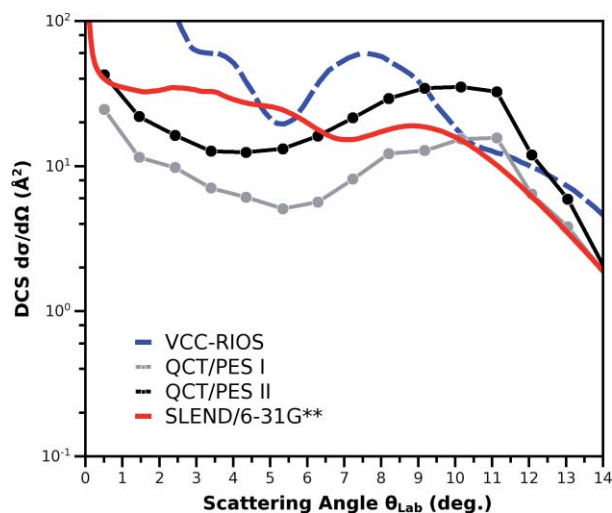


FIG. 9. Differential cross sections for the  $H^+ + N_2(v_i = 0) \rightarrow H^+ + N_2(v_f = 1)$  inelastic channel at  $E_{Lab} = 30$  eV vs. scattering angle: SLEND/6-31G\*\*, VCC-RIOS, (see Ref. 17) QCT/PES I and QCT/PES II (see Ref. 16) results. The last three values have been normalized as in Fig. 8.

31G\*\*, VCC-RIOS,<sup>17</sup> and QCT (Ref. 16) calculations. Again, the VCC-RIOS and QCT DCS, originally reported in arbitrary units, have been normalized following the criteria used in Fig. 8. No experimental DCS are available for the considered channel and only a comparison among theoretical results is possible. Figure 9 shows that the three types of inelastic DCS differ somewhat among themselves. Perceptibly, the SLEND/6-31G\*\* DCS are closer to the QCT ones than to the VCC-RIOS ones: a comparison similar to that among the average vibrational energy transfers from the same theories. The relative positions of the rainbow angle maxima of the inelastic DCS in Fig. 9 follow the same order of their counterparts in the elastic DCS in Fig. 8:  $\theta_{Lab}^{VCC-RIOS} < \theta_{Lab}^{SC,R,SLEND} < \theta_{Lab}^{QCT}$ .

## V. CONCLUDING REMARKS

The SLEND method<sup>19-21</sup> has been applied to the  $H^+ + N_2$  system at  $E_{Lab} = 30$  eV. As the simplest realization of the END theory,<sup>19-21</sup> SLEND adopts a classical-mechanics description for the nuclei and a single-determinantal wavefunction for the electrons. In this study, SLEND is associated with a canonical CS procedure<sup>14,31,36</sup> to reconstruct vibrational state-to-state properties from the SLEND classical mechanics. The primary goal of this study is to reproduce the main results of the seminal experiment on  $H^+ + N_2$  at  $E_{Lab} = 30$  eV by Krutein and Linder<sup>5</sup> and to simulate dynamical details and properties that are not accessible in that experiment. A secondary goal of this study is to compare the SLEND results on  $H^+ + N_2$  at  $E_{Lab} = 30$  eV with those obtained with two alternative theoretical methods: VCC-RIOS (Ref. 17) and QCT.<sup>16</sup>

The SLEND simulations were performed with three atomic basis sets: STO-3G, 6-31G, and 6-31G\*\*, to investigate their effect on the results. While in previous studies SLEND/STO-3G rendered some acceptable results,<sup>22,25</sup> this

investigation indicates that the choice of a minimal basis set should be made cautiously. SLEND/STO-3G predicts excessive  $N_2$  collision-induced dissociation and overestimates the rainbow scattering angle and the average vibrational energy transfer. The last two shortcomings prevent SLEND/STO-3G from providing acceptable  $H^+$  energy loss spectra and vibrational state-to-state DCS. In contrast, SLEND/6-31G and /6-31G\*\* predict reasonable  $N_2$  dissociations and render rainbow angles and average vibrational energy transfers in good agreement with their experimental counterparts. Furthermore, SLEND/6-31G\*\* predicts  $H^+$  energy loss spectra and elastic DCS in good agreement with the experimental results. The correctness of the SLEND/6-31G\*\* vibrationally resolved properties is due to the appropriateness of the canonical CS procedure with the moderately anharmonic  $N_2$  at  $v_f = 0 - 1$  and to the accuracy of the SLEND/6-31G\*\* vibrational energy transfer, which is the critical input of the canonical CS Poisson distribution, Eq. (8). In addition, the SLEND/6-31G and /6-31G\*\* results compare well with the VCC-RIOS and QCT results obtained at a higher computational cost (elaborate MRDCI PESs in both methods, costly quantum nuclear treatment in VCC-RIOS). Notably, SLEND/6-31G\*\* and QCT average vibrational energy transfers agree better with the experimental results than their VCC-RIOS counterpart. Finally, SLEND/6-31G\*\* provides elastic DCS whose rainbow angle maximum agrees much better with the experimental result than those from the VCC-RIOS and QCT DCS. More sophisticated versions of END, such as the END/KSDFT (Ref. 41) and the multi-configuration END (Ref. 37) methods, can simulate more accurately some aspects of the present system (e.g., the  $N_2$  vibrations with both methods, the  $N_2$  dissociations with the second) and therefore provide more precise results. Those END versions will be applied to the present system in the future.

## ACKNOWLEDGMENTS

All the present simulations were conducted at the Texas Tech University High Performance Computer Center (TTU HPCC). This material is based upon work partially supported by the National Science Foundation under Grant No. CHE-0645374 (CAREER), and by the Robert A. Welch Foundation under Grant No. D-1539. Also, acknowledgement is made to the donors of The American Chemical Society Petroleum Research Fund for partial support of this research.

<sup>1</sup>G. Niedner, M. Noll, J. P. Toennies, and C. Schlier, *J. Chem. Phys.* **87**(5), 2685 (1987).

<sup>2</sup>U. Hege and F. Linder, *Z. Phys. A* **320**, 95 (1985).

<sup>3</sup>H. Udseth, C. F. Giese, and W. R. Gentry, *J. Chem. Phys.* **60**(8), 3051 (1974).

<sup>4</sup>F. A. Gianturco, U. Gierz, and J. P. Toennies, *J. Phys. B* **14**(4), 667 (1981).

<sup>5</sup>J. Krutein and F. Linder, *J. Chem. Phys.* **71**(2), 599 (1979).

<sup>6</sup>M. Noll and J. P. Toennies, *J. Chem. Phys.* **85**(6), 3313 (1986).

<sup>7</sup>B. Friedrich, F. A. Gianturco, G. Niedner, M. Noll, and J. P. Toennies, *J. Phys. B* **20**, 3725 (1987).

<sup>8</sup>B. Friedrich, G. Niedner, M. Noll, and J. P. Toennies, *J. Chem. Phys.* **87**(9), 5256 (1987).

<sup>9</sup>G. Niedner, M. Noll, and J. P. Toennies, *J. Chem. Phys.* **87**(4), 2067 (1987).

<sup>10</sup>Y. N. Chiu, B. Friedrich, W. Maring, G. Niedner, M. Noll, and J. P. Toennies, *J. Chem. Phys.* **88**(11), 6814 (1988).

- <sup>11</sup>N. Aristov, G. Niednerschatteburg, J. P. Toennies, and Y. N. Chiu, *J. Chem. Phys.* **95**(11), 7969 (1991).
- <sup>12</sup>U. Gierz, M. Noll, and J. P. Toennies, *J. Chem. Phys.* **83**(5), 2259 (1985).
- <sup>13</sup>M. Baer, G. Niednerschatteburg, and J. P. Toennies, *J. Chem. Phys.* **91**(7), 4169 (1989).
- <sup>14</sup>J. A. Morales, A. C. Diz, E. Deumens, and Y. Öhrn, *Chem. Phys. Lett.* **233**(4), 392 (1995); *J. Chem. Phys.* **103**(23), 9968 (1995).
- <sup>15</sup>A. Dalgarno and J. H. Black, *Rep. Prog. Phys.* **39**, 573 (1976); E. Herbst, D. K. Bohme, J. D. Payzant, and H. I. Schiff, *Astrophys. J.* **201**, 603 (1975).
- <sup>16</sup>T. Ritschel, S. Mahapatra, and L. Zulicke, *Chem. Phys.* **271**(1–2), 155 (2001).
- <sup>17</sup>F. A. Gianturco, S. Kumar, T. Ritschel, R. Vetter, and L. Zulicke, *J. Chem. Phys.* **107**(17), 6634 (1997).
- <sup>18</sup>L. Sun and W. L. Hase, in *Reviews in Computational Chemistry*, edited by K. B. Lipkowitz, R. Larter, and T. R. Cundari (Wiley, New York, 2003), vol. 19, pp. 79.
- <sup>19</sup>E. Deumens, A. Diz, R. L. Longo, and Y. Öhrn, *Rev. Mod. Phys.* **66**(3), 917 (1994).
- <sup>20</sup>E. Deumens and Y. Öhrn, *J. Chem. Soc., Faraday Trans.* **93**(5), 919 (1997).
- <sup>21</sup>E. Deumens and Y. Öhrn, *J. Phys. Chem. A* **105**(12), 2660 (2001).
- <sup>22</sup>D. Jacquemin, J. A. Morales, E. Deumens, and Y. Öhrn, *J. Chem. Phys.* **107**(16), 6146 (1997).
- <sup>23</sup>M. Hedström, J. A. Morales, E. Deumens, and Y. Öhrn, *Chem. Phys. Lett.* **279**, 241 (1997).
- <sup>24</sup>S. A. Malinovskaya, R. Cabrera-Trujillo, J. R. Sabin, E. Deumens, and Y. Öhrn, *J. Chem. Phys.* **117**(3), 1103 (2002).
- <sup>25</sup>J. A. Morales, B. Maiti, Y. Yan, K. Tsereteli, J. Laraque, S. Addepalli, and C. Myers, *Chem. Phys. Lett.* **414**, 405 (2005).
- <sup>26</sup>B. Maiti, R. Sadeghi, A. Austin, and J. A. Morales, *Chem. Phys.* **340**(1–3), 105 (2007).
- <sup>27</sup>B. Maiti, P. M. McLaurin, R. Sadeghi, S. A. Perera, and J. A. Morales, *Int. J. Quantum Chem.* **109**, 3026 (2009).
- <sup>28</sup>R. Cabrera-Trujillo, Y. Öhrn, E. Deumens, J. R. Sabin, and B. G. Lindsay, *Phys. Rev. A* **66**, 042712 (2002).
- <sup>29</sup>R. S. Gao, L. K. Johnson, C. L. Hakes, K. A. Smith, and R. F. Stebbings, *Phys. Rev. A* **41**, 5929 (1990).
- <sup>30</sup>J. R. Klauder and B. S. Skagerstam, *Coherent States, Applications in Physics, and Mathematical Physics* (World Scientific, Singapore, 1985).
- <sup>31</sup>J. A. Morales, *Mol. Phys.* **108**, 3199 (2010).
- <sup>32</sup>C. F. Giese and W. R. Gentry, *Phys. Rev. A* **10**(6), 2156 (1974).
- <sup>33</sup>P. Kramer and M. Saraceno, *Geometry of The Time-Dependent Variational Principle in Quantum Mechanics*, 1st ed. (Springer-Verlag, New York, 1981).
- <sup>34</sup>H. Goldstein, *Classical Mechanics*, 2nd ed. (Addison-Wesley, Reading, MA, 1980).
- <sup>35</sup>D. J. Thouless, *Nucl. Phys.* **21**, 225 (1960).
- <sup>36</sup>J. A. Morales, E. Deumens, and Y. Öhrn, *J. Math. Phys.* **40**(2), 766 (1999).
- <sup>37</sup>E. Deumens, Y. Öhrn, and B. Weiner, *J. Math. Phys.* **32**(5), 1166 (1991).
- <sup>38</sup>C. Cohen-Tannoudji, B. Diu, and F. Laloë, *Quantum Mechanics* (Wiley-Interscience, New York, 1977).
- <sup>39</sup>I. N. Levine, *Quantum Chemistry*, 6th ed. (Prentice Hall, Upper Saddle River, NJ, 2008).
- <sup>40</sup>J. A. Morales, *J. Phys. Chem. A* **113**, 6004 (2009).
- <sup>41</sup>S. A. Perera, P. M. McLaurin, T. V. Grimes, and J. A. Morales, *Chem. Phys. Lett.* **496**(1–3), 188 (2010).
- <sup>42</sup>M. S. Child, *Molecular Collision Theory*, 1st ed. (Dover, New York, 1984).
- <sup>43</sup>J. N. L. Connor and D. Farrelly, *J. Chem. Phys.* **75**(6), 2831 (1981).